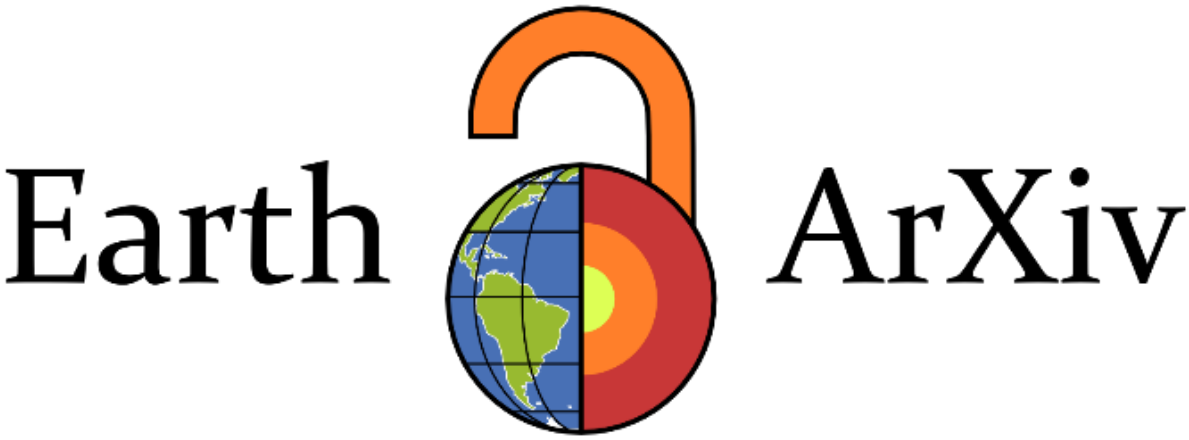

Dual and divergent formation pathways govern the composition and origins of mineral-associated organic carbon

Hongfei Liu[1], Carson Thompson[2], Chao Liang[3], Amy M. McKenna[4], Fu Chen[5], and Mengqiang Zhu[1]*

[1]Department of Geology, University of Maryland, College Park, MD 20742, USA

[2]Department of Ecosystem Science and Management, University of Wyoming, Laramie, WY 82071, USA

[3]Institute of Applied Ecology, Chinese Academy of Sciences, Shenyang, 110016, China

[4]National High Magnetic Field Laboratory, Florida State University, Tallahassee, FL 32310, USA

[5]Department of Chemistry and Biochemistry, University of Maryland, College Park, MD 20742, USA

* Corresponding author: Mengqiang Zhu

Email: mqzhu@umd.edu

Author Contributions: M.Z. and H.L. conceptualized and designed the study. H.L. and C.T. conducted data collection and analysis. C.L. contributed to conceptual development. A.M.M. collected FT-ICR-MS data and contributed to data processing. F.C. assisted with data collection and analysis of ^{13}C CPMAS NMR spectra. H.L. and M.Z. wrote the manuscript with inputs from C.L.

Competing Interest Statement: The authors declare no competing interest.

Classification: Biological Sciences, Environmental Sciences.

Keywords: Soil carbon, Mineral-associated organic matter, Adsorption, Aggregation, Chemical composition.

Abstract

Mineral-associated organic matter (MAOM) is the largest and most stable soil carbon reservoir, playing a central role in soil health and climate mitigation. Yet, quantitative understanding is lacking for the two fundamental processes forming MAOM— adsorption of dissolved organic matter and aggregation of insoluble organic particles—and how each pathway incorporates plant- versus microbial-derived carbon. Analyzing soils from diverse ecosystems across North America, we found that both pathways substantially contributed to MAOM, with adsorption accounting for 11–96% and aggregation for 5–89% of total MAOM carbon, depending strongly on environmental context. Adsorbed MAOM was consistently dominated by plant-derived aromatic compounds and exhibited Langmuir-type saturation dynamics, whereas aggregated MAOM was consistently enriched in non-aromatic, microbial residues and did not saturate. On average, plant-derived carbon constitutes 59% of total MAOM carbon. Despite substantial environmental shifts in pathway dominance, the molecular composition within each fraction remained remarkably consistent across ecosystems, indicating strong mineral and microbial filtration effects. These findings provide pathway-specific parameters for refining soil-carbon models and offer practical guidance for management strategies targeting long-term carbon sequestration.

Significance Statement

Mineral-associated organic matter (MAOM) holds most of the stabilized carbon stored in soils worldwide, yet the mechanisms that concentrate plant- and microbial-derived material in this stable pool remain poorly resolved. Using a continent-wide soil survey and state-of-the-art molecular characterization, we show that MAOM assembles by two contrasting pathways: adsorption of soluble, plant-derived aromatics onto mineral surfaces and aggregation of insoluble, primarily microbially derived residues within fine microaggregates. The balance between these pathways shifts predictably with soil depth, moisture, and mineralogy—adsorption dominating deep or humid soils and aggregation dominating surface or arid soils. This dual-pathway framework reshapes our understanding of soil-carbon stabilization and offers actionable targets for managing soils to maximize long-term carbon storage under a changing climate.

Main Text

Introduction

Soil organic matter (SOM) is a major global sink for atmospheric carbon and underpins both soil fertility and climate regulation (1). Yet, SOM is highly vulnerable to climate and land-use changes due to its sensitivity to environmental conditions (2, 3). Close contact with soil minerals—especially silt and clay—protects SOM from microbial decomposition, creating mineral-associated organic matter (MAOM), which stores ~65 % of global soil organic carbon (SOC) (1, 4). Boosting MAOM accumulation is therefore central to efforts that seek to build SOC, preserve soil health, and curb climate change. However, we lack a clear, quantitative picture of the two key processes that create MAOM—molecular-scale adsorption of dissolved organic matter versus micrometer-scale aggregation of insoluble particles—and of how each process incorporates plant- versus microbial-derived carbon. Resolving these gaps demands systematic, cross-ecosystem studies that move beyond site-specific observations to establish general, predictive principles for global carbon management and modelling.

Soil organic carbon (SOC) models typically represent MAOM formation as Langmuir-type adsorption (5–7). The Langmuir model describes a scenario where the amount of organic matter adsorbed onto a mineral surface increases with dissolved organic matter concentration but eventually levels off once adsorption sites are saturated (8, 9). Thus, those MAOM models implicitly assume all organic inputs are soluble (10, 11). This overlooks a key distinction: soluble compounds bind to minerals at molecular scales via adsorption, whereas insoluble organic particles form nano– to micrometer scale solid–solid associations through aggregation, a process that does not saturate or conform to Langmuir dynamics (12–14). Although some SOC models consider adsorption and aggregation separately, empirical data quantifying their relative contributions to MAOM formation are lacking and how to parameterize the aggregation pathway is unknown (15). Moreover, the carbon stabilized by each pathway likely differs in persistence, environmental dependence, and sensitivity to disturbance (16–18). Taken all together, disentangling and quantifying adsorption versus aggregation is therefore essential for prediction and management of MAOM dynamics.

70 Plant- and microbial-derived carbon also enter MAOM by different routes. Although MAOM was historically
71 treated as amorphous “humus,” it is now known to contain discrete compounds that can be traced to either
72 plants or microbes (14, 19, 20). Microbial-centric models—built largely on solid-state ^{13}C NMR
73 spectroscopic analyses that show little aromatic carbon—therefore argue that MAOM is dominated by
74 microbial inputs (2, 20–23). Yet amino-sugar biomarkers and complementary chemical assays increasingly
75 reveal substantial plant-derived aromatics in MAOM (24–26); indeed, amino-sugar data indicate that
76 microbial products account for only 11–57 % of MAOM-C across soils and land uses (27). Much of this
77 discrepancy stems from the standard hydrogen-fluoride (HF) pretreatment used to remove iron before NMR
78 analysis. HF pretreatment is widely used because iron and other paramagnetic metals interfere with NMR
79 signals, reducing spectral quality. However, HF also dissolves other oxides and phyllosilicates, and along
80 with Fe minerals, they are the main sorbents for dissolved organic matter. The dissolution releases
81 aromatic, plant-derived compounds into solution, leaving mainly insoluble microbial residues for NMR
82 characterization (28, 29). In acidic forest soils, HF removed up to 76 % of clay-associated C, almost entirely
83 plant-derived aromatics (30). Such methodological bias likely inflates the apparent microbial share and
84 understates the plant contribution to MAOM.

85 Building on this evidence, we propose that MAOM forms through two distinct, source-specific pathways
86 (conceptual diagram, Fig. 1). The soluble, now-adsorbed fraction is dominated by plant-derived aromatic
87 compounds, whereas the insoluble, aggregated fraction is enriched in microbial necromass. Because
88 adsorption and aggregation—and their associated carbon pools—respond differently to abiotic and biotic
89 drivers, we further hypothesize that the relative importance of these pathways, and thus the balance
90 between plant- and microbial-derived carbon in MAOM, shifts markedly along environmental gradients.

91 To test these hypotheses, we paired continent-wide sampling from the National Ecological Observatory
92 Network (NEON) with HF fractionation to split MAOM into soluble (HF-DOC) and insoluble (HF-ResC)
93 pools, followed by high-resolution molecular analyses. NEON sites span broad climatic, ecological and
94 edaphic gradients (*SI Appendix*, Fig. S1), including variations in temperature, precipitation, vegetation, and

soil types. This diversity provides a powerful natural laboratory for capturing a wide range of environmental conditions, thereby enhancing the generalizability and robustness of hypothesis testing. MAOM fractions were isolated using combined density and size separation (Methods). The HF-DOC represents adsorbed organic matter, whereas HF-ResC captures material occluded within microaggregates (<53 μm) that resist dispersion (19, 31). We quantified the two pools in 180 A- and B-horizon samples; detailed molecular profiling was conducted on the uppermost horizons. Molecular composition of HF-DOC was analyzed using electrospray ionization 21-Tesla Fourier-transform ion cyclotron resonance mass spectrometry (ESI FT-ICR-MS), and HF-ResC was characterized using solid-state ^{13}C cross-polarization magic-angle-spinning NMR spectroscopy coupled with molecular mixing modeling. Consistent with our predictions, the dominant pathway shifted with environment: adsorption prevailed in deep, low-SOC soils or humid regions, whereas aggregation dominated surface, high-SOC soils or arid sites. Nevertheless, within each fraction the composition and sources were remarkably similar across ecosystems—soluble MAOM was consistently rich in aromatics exclusively of plant origin, while insoluble MAOM was dominated by non-aromatic, microbial carbon.

Results and Discussion

Contributions of adsorption versus aggregation/attachment to MAOM formation

The relative contributions of adsorption versus aggregation/attachment to MAOM formation were ecosystem-specific and varied widely across the continental scale (Fig. 2*A*). HF-DOC contributed 10.8–95.5% of total MAOC (mean: 52.5%), while HF-ResC accounted for 4.5–89.2% (mean: 47.5%) of MAOC. This wide variability in the contributions of each fraction underscores the importance of considering both adsorption and aggregation pathways in carbon modeling and soil management strategies tailored to local environmental conditions. Although the concentrations of both fractions increased with total MAOC concentration (g C per kg of MAOM material; MAOM material - the combined mass of MAOC, silt, and clay; Fig. 2*B*), they displayed distinct relationships with MAOC levels. HF-DOC followed a Langmuir adsorption

model and exhibited a saturation behavior: its concentration increased and reached a plateau as the MAOC concentration increased. The saturation suggests a limit to how much dissolved organic matter can be stabilized via adsorption, which is critical for predicting carbon stabilization thresholds across ecosystems with varying mineral surface areas and organic matter inputs. In contrast, the concentration of HF-ResC did not demonstrate any sign of saturation, which increased nonlinearly, accelerating with increasing MAOC. Our observation is consistent with that adsorption saturates due to decreasing availability of mineral surface areas as organic loading increases (32), whereas aggregation, probably attachment as well, is less constrained by surface area and can continue as long as organic inputs provide sufficient binding agents, such as EPS and mucilage (14). The observation thus validates our assumption that HF-DOC represents the adsorbed fraction and HF-ResC the aggregated fraction. Due to their different dependences on mineral surface areas, adsorption declined, and aggregation/attachment increased in relative importance to MAOM formation with rising MAOC concentrations, particularly in the wetter ecosystems (MAP/PET > 0.65, Fig. 2*C*; MAP: mean annual precipitation, PET: potential evapotranspiration). Thus, at the initial stage of MAOC accrual where MAOC concentration is relatively low, adsorption of dissolved organic matter contributes more than aggregation of insoluble organic particles.

Key controlling environmental drivers on contributions of pathways to MAOM formation

Effective soil moisture (MAP – PET), a climate factor, and soil depth primarily control the dominant pathway of MAOM formation by regulating soil pH and mineral availability (Fig. 2*D*). Adsorption-dominated soils with low MAOC concentrations are typically found in humid environments and deeper layers, where adsorptive minerals, such as metal oxides, were abundant and pH was low (Fig. 2*D*). Low pH enhances the positive surface charge of metal oxides, increasing their affinity for negatively charged dissolved organic compounds, while the high surface area of metal oxides provides ample binding sites for adsorption. These soils were often low in the total organic C concentration as well (*SI Appendix*, Fig. S2). These conditions favor DOM adsorption but suppress microbial activity (33, 34). Reduced microbial activity limits the production of microbial necromass—insoluble residues resulting from microbial cell death and decay—that

144 are essential precursors for the aggregation/attachment pathway (14). Without sufficient microbial turnover,
145 there are fewer binding agents like extracellular polymeric substances to facilitate organic matter
146 aggregation. As a result, DOM, once entering the soils, is quickly adsorbed onto mineral surfaces rather
147 than microbially assimilated to produce insoluble microbial necromass for the aggregation/attachment
148 pathway (35). Moreover, in wetter climates, dissolved organic matter, not insoluble ones, is the main carbon
149 source capable of percolating into subsoil layers in wetter environments (36, 37), further enhancing the
150 dominance of adsorption in deeper soils. In contrast, dry ecosystems with a low net primary productivity
151 and limited moisture restrict both DOC production and its vertical transport, thereby reducing adsorption
152 (36, 38). This limitation in DOC transport reduces the input of carbon substrates into subsoils, constraining
153 the formation and persistence of MAOM and ultimately lowering the potential for long-term carbon
154 sequestration in these environments. In summary, adsorption prevailed in deep, low-SOC soils and wetter
155 climates, while aggregation/attachment dominated in surface, high-SOC soils and drier regions, highlighting
156 how environmental context shapes the pathways of MAOM formation.

157 **Pathway-specific chemical composition of organic C**

158 Aromatic compounds, including lignin, tannin and condensed aromatics comprised 76.8–99.0% of the HF-
159 DOC molecules (Fig. 3*A*), indicating they played a predominant role in MAOM formation through adsorption.
160 Lignin exhibited the highest relative abundance (31.6–66.1%), followed by condensed aromatics (9.5–
161 53.6%) and tannins (6.8–19.1%). This general pattern was consistent across most sampled ecosystems,
162 though the relative contributions of each aromatic compound varied somewhat with environmental
163 conditions such as MAP and soil pH. The dominance of these aromatics in HF-DOC is consistent with
164 adsorption-induced molecular fractionation by which aromatics in soil solution are preferentially adsorbed
165 onto mineral surfaces compared to non-aromatic compounds (39–41). Microbial decomposition may further
166 enhance accumulation of aromatics on mineral surfaces via adsorption. Non-aromatic compounds, such as
167 celluloses, hemicellulose, and amino acids are preferentially and readily mineralized during decomposition,
168 leaving behind lignin and tannins (12, 42). These lignin and tannin compounds, as well as condensed

aromatics, are further modified by microbes and other soil processes, thereby enhancing their solubility and adsorption reactivity on mineral surfaces (1, 12, 43). Lignin and tannin in soil are exclusively derived from plant sources (44), while condensed aromatic compounds primarily originate from the incomplete combustion of vegetation during wildfires or the condensation of plant decomposition byproducts (45). The results support the zonal structure model, which was developed primarily based on laboratory simulation studies (10, 46), by demonstrating that the adsorbed fraction, approximating the OM in the combined contact and hydrophobic-interaction zones, is rich in aromatic compounds. The zonal structure model proposes that organic matter associates with minerals in spatially distinct zones, where the contact zone involves strong, specific interactions and the hydrophobic-interaction zone reflects weaker, nonspecific adsorption driven by molecular properties such as aromaticity (46). To summarize, due to compound preference, mineral adsorption and microbial processing act as filters, jointly resulting in the adsorption pathway primarily stabilizing plant-derived aromatic C compounds.

In contrast to the dominance of aromatics in the adsorbed MAOM fraction, the chemical composition of the aggregated/attached fraction was dominated by non-aromatic compounds. Alkyl C and O-alkyl C were the predominant functional groups, comprising 25.3–61.6% and 18.3–38.8% of HF-ResC, respectively (Fig. 3*C*). N-alkyl and methoxy C (0.5–15.3%) and aromatic C (4.0–17.9%) were present in lower proportions, yet they still exceeded the levels of Di-O-alkyl C, phenolic C, and amide/carboxyl C (Fig. 3*C*). A molecular mixing model was employed to estimate the relative abundances of biochemical classes in HF-ResC (47, 48). This approach allows for the deconvolution of overlapping NMR signals into recognizable biochemical groups, providing a semi-quantitative assessment of MAOM molecular composition. However, it relies critically on assumptions linking chemical shift regions to specific biomolecule types, derived primarily from idealized reference materials, which may not fully capture molecular complexity of MAOM (47, 48). Results show that lipids (23.8–44.1%), carbohydrates (13.9–32.2%), and proteins (16.4–24.7%) were the most abundant biochemical classes, followed by lignin (10.1–14.5%) and condensed aromatics (3.2–14.1%) (Fig. 3*D*).

While lignin and condensed aromatics originate unambiguously from plants, the sources of non-aromatic carbon in HF-DOC and HF-ResC are ambiguous, as both plants and microbes can produce these compounds. In HF-DOC, the carbohydrate abundance strongly correlated with amino sugars ($r = 0.52$, $p < 0.0001$; *SI Appendix*, Fig. S3 and S4), the biomarkers of microbial residues (49), suggesting microbial origins of the adsorbed carbohydrates. Similarly, the relative abundance of carbohydrates in HF-ResC positively correlated with the amino sugar-to-MAOC ratio of MAOM (*SI Appendix*, Fig. S5), suggesting microbial origins for aggregated and attached carbohydrates as well. These findings align with prior work showing that microbial-derived carbohydrates accumulated in MAOM (50, 51), while plant-derived ones (e.g., cellulose and hemicellulose) were rapidly decomposed (52–54). Microbial-derived carbohydrates are more persistent likely because they are often embedded in microbial cell walls and extracellular matrices, which can physically protect them from enzymatic attack and facilitate interactions with minerals that enhance stabilization.

Lipids and proteins differed from carbohydrates in their sources, contingent on MAOM formation pathways. In HF-DOC, their positive correlations with amino sugars (*SI Appendix*, Fig. S3 and S4) suggest microbial origins, likely reflecting rapid microbial processing of plant-derived compounds into soluble forms (55, 56). In HF-ResC, a principal component analysis revealed lipids and proteins clustered together but separated from carbohydrates (*SI Appendix*, Fig. S6), with abundances uncorrelated to amino sugar-to-MAOC ratios (*SI Appendix*, Fig. S5). We speculate that the aggregated/attached lipid and protein compounds in MAOM originate from a mixture of plant and microbial sources (27, 57). Functionally, lipids and proteins contribute to MAOM stabilization through their hydrophobic and nitrogen-rich structures, respectively. The hydrophobic nature of lipids can reduce decomposition rates by limiting microbial access, while nitrogen-rich proteins (insoluble here) may form highly stable aggregates with mineral particles (12, 14, 58). Angst et al. (27) estimated that plant-derived lipids (e.g., long-chain n-alkanoic acids and cutin/suberin derivatives) account for 2–10% of MAOC. For our calculations, we therefore adopt the midpoint of that range, 6.0%, as the average contribution from plant-derived lipids across ecosystems. Given our observed lipid

contributions (8.7–31.3%; mean: 18.4%), we estimate that roughly 30% of lipids/proteins in aggregated/attached MAOM were plant-derived.

Overall, we estimate that plant-derived materials account for 76.8–99.0% and microbial-derived materials for 1.0–23.2% of adsorbed MAOC (Fig. 3*E*, *SI Appendix*, Fig. S7), and for 28.0 - 43.1% and 56.9 - 72.0%, respectively, of aggregated/attached MAOC (Fig. 3*E*, *SI Appendix*, Fig. S8). Merging the adsorbed and aggregated/attached fractions together, plant-derived materials dominated with contributions ranging from 40.2% to 80.7% (mean: 59.1%), whereas microbial-derived materials contribute 19.3–59.8% (mean: 40.9%) of bulk MAOC (Fig. 3*E*, *SI Appendix*, Fig. S9). Despite uncertainties in distinguishing plant- versus microbial-derived contributions to specific biochemical classes within MAOC, aromatic compounds (lignin, tannins, and condensed aromatics) derived exclusively from plants still accounted for 29.5–77.5% (mean: 51.9%) of bulk MAOC (*SI Appendix*, Fig. S9).

Our results do not align with prior studies using ^{13}C NMR spectroscopy, which reported that bulk MAOM primarily consisted of polysaccharides and aliphatic compounds (14, 59, 60). As discussed earlier, these studies misinterpreted their results as the pretreatment of MAOM materials with 10% HF to remove Fe prior to NMR analyses had already removed the soluble organic carbon. Future studies could address this bias by using carbon K-edge X-ray absorption spectroscopy which is not subject to influence by Fe or other elements (61).

Key controlling environmental drivers on the organic C composition of each pathway

Environmental drivers—including soil pH, MAP, MAT, and clay content—differentially regulated the contributions of aromatic compounds to MAOM fractions. Backward stepwise regression identified soil pH and MAP as the strongest predictors of aromatic enrichment in the adsorbed MAOM fraction: higher MAP (Fig. 4*A*) and lower pH (Fig. 4*B*) both increase Fe and Al oxide availability (12), promoting selective adsorption of carboxyl-rich aromatics (39–41). The share of aromatic compounds in the aggregated/attached MAOM fraction declined with decreasing pH, clay content, and MAT (Fig. 4*C*–*E*).

Lower pH favors fungal over bacterial communities, accelerating aromatic breakdown (62). Fungi possess enzymatic systems, such as lignin peroxidases and laccases, that are particularly efficient at degrading complex aromatic structures like lignin (62). As a result, shifts toward fungal dominance in low-pH soils enhance the decomposition of plant-derived aromatics, reducing their persistence in the aggregated/attached MAOM fraction. Although higher MAT boosts litter inputs—and thus aromatic C supply (*SI Appendix*, Fig. S6)—it also reduces microbial carbon use efficiency, while lipid oxidation remains especially temperature-sensitive due to its high activation energy (63). In clay-rich soils, enhanced moisture retention, particularly in dry lands, and pH buffering protect microbial communities from stressors (10, 12, 64), encouraging necromass recycling and the stabilization of plant-derived, aromatic compounds (64–66).

Implication for SOC sequestration and stability

Our continental-scale analysis shows that MAOM forms via two distinct pathways—adsorption of plant-derived aromatics and aggregation/attachment of microbial residues — whose balance shifts with effective soil moisture and depth but their molecular fingerprints remain remarkably consistent across ecosystems. This dual-pathway perspective resolves the long-standing plant-versus-microbe debate by demonstrating that plant inputs dominate the soluble, adsorbed pool, whereas microbial carbon prevails only in the insoluble, aggregated fraction (Fig. 1). The finding overturns the contentious assumption that microbial necromass is the chief MAOM source and restores the key role of plant compounds in long-term soil-carbon storage (20, 21, 67).

Our findings provide empirical evidence to refine process-based SOC models focused on MAOM dynamics. The two identified fractions—soluble, adsorbed organic carbon and insoluble, aggregated residues—likely correspond to the dynamic and stable pools represented in SOC models such as MEMS 2.0 (68), a correspondence that future radiocarbon carbon studies can further validate. Unlike current models such as COMISSION 2.0 and JSM, which represent MAOM formation as a single unified adsorption process (5, 6), our results advocate separating adsorption and aggregation/attachment into distinct model sub-modules, each with unique sources, kinetics, and environmental responses, such as in Millennial model V2 (15).

Adsorption modules should retain a Langmuir-type saturation model specifically calibrated for plant-derived aromatics. In contrast, aggregation modules should employ a non-saturating model (e.g., Fig. 2*b*), explicitly linking carbon stabilization to microbial necromass production (15). Adopting this conceptual distinction will enhance our mechanistic understanding of MAOM formation and saturation (69), significantly improving projections of SOC responses to environmental change and land management.

Effective soil carbon management should strategically target the dominant MAOM formation pathway based on local environmental conditions. Pathway-specific strategies can enhance MAOM where it is most limiting. In soils nearing adsorption saturation, practices that build fine particulate matter and promote aggregation—crop-residue retention, organic amendments, reduced tillage, continuous grass cover, diverse forest litter—will shift carbon toward the microbial, aggregated pool (70–74). Conversely, in deep or low-SOC profiles where adsorption capacity is unsaturated, maintaining soil moisture, fostering deep-rooted plants, encouraging bioturbation (e.g., earthworms), and controlled deep mixing can deliver both dissolved and particulate carbon to depth (36, 70, 75–77), boosting MAOM by both pathways. Because some interventions (e.g., deep ploughing) risk structural disruption or erosion, site-specific monitoring is essential to balance carbon gains against potential losses.

Materials and methods

Study sites and sampling

A total of 43 terrestrial sites of NEON were selected for the study (*SI Appendix*, Fig. S1). These sites span 20 ecoclimatic domains, representing diverse landforms, vegetation types, climatic conditions, and ecosystem dynamics across the United States (78). At each site, NEON sampled soils by horizon to depths of up to 2 meters in non-permafrost areas and up to 3 meters in Alaskan sites. A single, temporary soil pit—the “Megapit”—was used, with its location determined by the dominant soil type, vegetation, and topography surrounding the NEON flux tower to ensure it accurately represented nearby soil sensor sites. Basic physical and chemical properties were measured by NEON following standardized protocols to minimize

sampling and analytical biases. This study focused exclusively on samples from the A and B horizons collected from the Megapit, while C horizon samples (e.g., saprolite) were excluded due to their low SOC content. For Gelisols with extensive O horizons, the first two mineral sub-horizons closest to the surface were included in the analysis—for example, Cgjj/Oajj and Cgjff/Oajjf in BARR; Bg/Oajj and Cg in BONA; A/Cjj and Cjjf in HEAL; and Bw and BC in TOOL. Although the Megapit design lacked site replicates, previous research has shown it effectively captures significant SOC patterns at the continental scale (63, 79, 80).

Physical fractionation of soil organic matter

Following Leuthold et al. (2022), SOM was separated into POM and MAOM using the combined density (1.85 g cm^{-3}) and size (53 µm) fractionation protocol (81). Approximately 5 g of air-dried soil (<2 mm) was first shaken with deionized (DI) water for 15 minutes and then centrifuged at 5000 rpm for 30 minutes. The supernatant was decanted and passed through a 0.45 µm PTFE filter, capturing the particulate material as the light POM fraction (density <1.85 g cm^{-3}). Next, 12 glass beads and 25 ml of sodium polytungstate (density 1.85 g cm^{-3}) were added to the remaining soil residue. The mixture was shaken for 18 hours to disperse soil aggregates and then centrifuged again at 5000 rpm for 30 minutes, separating it into a light fraction (light POM) and a heavy fraction (heavy POM and MAOM). The light fraction was rinsed thoroughly with DI water and dried at 60 °C to yield the light POM. The heavy pellet (density >1.85 g cm^{-3}) was rinsed repeatedly to remove residual sodium polytungstate and then wet sieved through a 53 µm mesh. This process separated heavy POM (particles >53 µm) from MAOM (particles <53 µm). The material passing through the sieve—comprising MAOM, silt, and clay—was collected separately from the heavy POM plus sand remaining on the sieve. These obtained light POM, heavy POM and MAOM fractions were dried at 60 °C in oven and ground to fine powders prior to HF extractions as described below.

Following Eusterhues et al. (2003), the MAOM fraction was further separated into HF-DOC and HF-ResC using HF extraction (28). First, 1 g of MAOM was treated with 10 mL of a 10% HF solution and shaken for 2 hours at room temperature. The suspension was then centrifuged at 5000 × g for 2 hours, and the

supernatant was transferred to a 50 mL centrifuge tube. This extraction step was repeated five times to ensure thorough dissolution of soil minerals. After extraction, the soil residues were rinsed five times with deionized water to remove salts and any residual HF. The combined supernatants were stored at –20 °C as HF-DOC, while the remaining soil residues (HF-ResC) were oven-dried at 60 °C and weighed for subsequent chemical analysis.

Total carbon and nitrogen concentrations in MAOM and HF-ResC samples were determined using an elemental analyzer (Laramie, WY, USA). For calcareous soils (pH > 6.5) with high inorganic carbon levels, the inorganic carbon in bulk MAOM was removed using HCl fumigation (82). The carbon concentration in HF-DOC samples was analyzed with a Shimadzu TOC analyzer. The carbon concentrations measured in HF-ResC and HF-DOC yielded comparable HF-DOC/MAOC ratios (data not shown). Consequently, this study reports the average of the two measured HF-DOC/MAOC values.

Twenty-One Tesla Fourier-Transform Ion Cyclotron Resonance Mass Spectrometry (FT ICR MS) analysis

Prior to the FT-ICR-MS analysis, HF-DOM samples from the uppermost A and B horizons were purified to remove dissolved ions—including SPT and metals—using solid phase extraction (SPE) with PPL cartridges, following standard protocols (83). First, the cartridges were preconditioned with acetone and methanol, then equilibrated with one cartridge volume of 0.1 M HCl. The extraction solution volume for each sample was adjusted to allow approximately 100 µg of carbon to pass through the cartridge by gravity. After sample loading, the cartridges were rinsed with 0.1 M HCl and dried with a gentle flow of N_2 gas. The organic matter retained on the cartridges was eluted with methanol followed by acetone. Finally, the purified HF-DOM samples were stored in the dark at - 20 °C until the FT-ICR-MS analysis.

The chemical composition of HF-DOM was determined using a custom-built 21-T ESI FT-ICR MS equipped with a hybrid linear ion trap and a dynamically harmonized ICR cell operated at 6 V, located at the National High Magnetic Field Laboratory in Tallahassee, FL (84–88). Sample solutions were infused via a

microelectrospray source (50 µm i.d. fused silica emitter) at 500 nL/min using a syringe pump. For negative ion formation, typical settings included an emitter voltage of –2.7 to –3.0 kV, an S-lens RF level of 45%, and a heated metal capillary at 350 °C. The instrument collected data over a mass range of 150–1100 Da. Mass spectral peak lists in adsorption mode were internally calibrated using 10–15 highly abundant homologous series (300 individual calibrants) across the molecular weight distribution via the "walking" calibration method (89). Peaks with a signal magnitude exceeding six times the baseline root-mean-square noise at m/z 500 were exported for analysis. Molecular formula assignments and data visualization were performed with PetroOrg© software, discarding any assignments with errors greater than 1 ppm. Formulas were assigned only to peaks with a signal-to-noise ratio of ≥ 6, following elemental constraints (C_{3-150}, H_{3-300}, N_{0-3}, O_{1-40}, S_{0-2}, P_{0-1}, $^{13}C_{0-2}$, $^{15}N_{0-1}$) with O/C ≤1.5 and H/C ≤2.5.

Molecular intensities from FT-ICR-MS measurements were normalized to the total detected intensity, enabling calculation of relative molecular intensities. This approach captures DOM molecular patterns more precisely than binary presence/absence methods (90). To analyze DOM composition, van Krevelen (VK) diagrams were generated by categorizing molecules into biochemical classes based on their molar H:C and O:C ratios (91): Amino sugar (2.2 ≥ H/C ≥1.5; 0.7 ≥ O/C >0.55), Carbohydrates (2.2 ≥ H/C ≥ 1.5; 1.05 ≥ O/C > 0.7), Condensed hydrocarbon (0.8 > H/C ≥ 0.2; 0.95 ≥ O/C ≥ 0), Lignin (1.5 > H/C ≥ 0.8; 0.65 ≥ O/C > 0.125), Lipid (2.5 ≥ H/C ≥1.5; 0.3 ≥ O/C > 0), Protein (2.3 ≥ H/C ≥1.5; 0.55 ≥ O/C > 0.3), Tannin (1.5 > H/C ≥0.8; 1.1 ≥ O/C > 0.65), Unsaturated hydrocarbon (1.5> H/C ≥0.8; 0.125 ≥ O/C ≥ 0).

^{13}C CPMAS NMR analysis and sample preparation

To elucidate the molecular structure of HF-ResC, 36 uppermost A horizon and 15 uppermost B horizon HF-Res samples were prepared for NMR analysis. Solid-state ^{13}C CPMAS NMR spectra were recorded at 23 °C using a Bruker AV NEO 500 MHz NMR spectrometer with a 3.2 mm H/F-X double resonance MAS probe. Each 60–130 mg MAOM sample was loaded into a 3.2 mm zirconium rotor capped with Kel-F to optimize carbon mass and signal intensity. A magic angle spinning (MAS) rate of 12 kHz was maintained for all

measurements. For the CP experiments, a ramped-amplitude contact pulse (100%) and rotor-synchronized Hahn echo were employed, with a contact time of 1.2 ms and a recycle delay of 2.0 s; composite pulse proton decoupling was applied during signal acquisition. Glycine was used as an external standard to calibrate pulse angles, chemical shifts, and Hartman–Hahn matching conditions.

The CPMAS ^{13}C NMR spectra for HF-treated samples were acquired using over 10,000 scans. After baseline correction, the spectra were divided into seven chemical shift regions—0–45 ppm, 45–60 ppm, 60–95 ppm, 95–110 ppm, 110–145 ppm, 145–165 ppm, and 165–215 ppm—corresponding to alkyl C, N-alkyl/methoxyl C, O-alkyl C, di-O-alkyl C, aromatic C, phenolic C, and amide+carbonyl C, respectively. A molecular mixing model was then applied to these integrated regions to estimate the relative abundances of six biochemical groups: carbohydrate, protein, lignin, lipid, carbonyl, and char (47, 48). The resulting solution defines the relative abundance of each chemical group (see detailed information in Text S2 and Table S2).

Data on soil physico-chemical properties, litter and root biomass, and climate data

The data on soil physicochemical properties were obtained from the NEON data portal for soil samples collected from each horizon within each Megapit. Soil texture was characterized by the following parameters: total sand percentage (0.047–2 mm), total silt percentage (0.002–0.047 mm), total clay percentage (<0.002 mm), fine silt percentage (0.002–0.02 mm), coarse silt percentage (0.02–0.05 mm), very fine sand percentage (0.047–0.105 mm), fine sand percentage (0.105–0.25 mm), medium sand percentage (0.25–0.5 mm), coarse sand percentage (0.5–1 mm), and very coarse sand percentage (1–2 mm). The soil chemical properties included total concentrations of carbon (C), nitrogen (N), sulfur (S), aluminum (Al), calcium (Ca), iron (Fe), potassium (K), magnesium (Mg), manganese (Mn), sodium (Na), phosphorus (P), and silicon (Si), along with pH, electrical conductivity, gypsum content, carbonate content, and ammonium acetate-extractable Ca, K, Mg, and Na. Additionally, ammonium acetate cation exchange capacity and potassium chloride (KCl) extractable Al and Mn were also measured. Concentrations of Fe

and aluminum in SRO phases and organo-metal complexes (termed Feox and Alox) were extracted with ammonium oxalate.

Data on litter biomass were sourced from the NEON data portal, collected using elevated 0.5 m^2 PVC traps at 33 NEON sites, including ABBY, BART, BALN, BONA, CLBJ, DEJU, DELA, GRSM, GUAN, HARV, HEAL, JERC, KONZ, LENO, MLBS, NIWO, ORNL, OSBS, PUUM, RMNP, SCBI, SERC, SJER, SOAP, SRER, STEI, TALL, TEAK, TREE, UKFS, UNDE, WREF, and YELL. The dry biomass weight of total litter and each functional group (seeds, needles, twig branches, woody material, mixed flowers, leaves, mixed, and others) was calculated in grams per trap.

This study utilizes root biomass data from the NEON data portal, with samples collected from three soil profiles in the Megapit at all sites except KONA and TOOL. While NEON root data were sampled at 10 cm depth increments, our soil samples were collected by genetic horizon. Therefore, adjustments were necessary to align the root biomass data with the sampling depths of the soil samples used for physicochemical analysis. The top and bottom depths of the genetic horizons were approximated to the nearest 10 cm intervals. For each Megapit at every site, root biomass measurements that fell within the adjusted depth ranges of the individual genetic horizons were aggregated to calculate the total root biomass for each horizon. The root biomass for each genetic horizon at each site was determined by combining and averaging the data from the three soil profiles.

The mean annual temperature (MAT) data used in this study were obtained from Hall et al., 2020. Mean annual precipitation (MAP) and potential evapotranspiration (PET) for each site were generated using the ClimateNA v.5.10 software package, available at https://tinyurl.com/ClimateNA, following the methodology described by Wang et al., 2016 (92). PET estimates were specifically derived using the temperature-driven Hargreaves method (93).

Statistical analyses

Data normality was evaluated with the Shapiro-Wilk test and variance homogeneity with Levene's test before performing one-way ANOVA (94, 95). Tukey's post hoc test then assessed the effects of soil horizon (A vs. B) on HF solubility, the relative abundance and biochemical index of HF-DOC, and the relative abundance of functional groups and biochemical classes in HF-ResC ($P < 0.05$) (96). We examined the correlations between OC concentration in MAOM material and HF solubility, HF-DOC, and HF-ResC using the Langmuir adsorption model, simple linear regression, and various nonlinear models (quadratic, exponential, power law, and logarithmic), selecting the best-fit model based on AIC. Before conducting backward stepwise regression, we used the variance inflation factor (VIF) from the R package "car" to assess multicollinearity among environmental variables (soil physicochemical properties, climatic characteristics, and vegetation properties). Variables with a VIF greater than 5 were excluded. The backward stepwise regression (using the R package "MASS") then identified the predictors for HF solubility, the proportion of aromatic compounds in HF-DOC, and the proportion of non-aromatic compounds in HF-ResC. Finally, we constructed a structural equation model (SEM) with the R package "piecewiseSEM" to evaluate the direct and indirect effects of environmental variables on HF solubility (97). Partial correlation analyses, following Grace et al. (2016), further addressed multicollinearity between the selected environmental variables and the compound proportions in HF-DOC and HF-ResC (98).

Acknowledgments

This work was partially supported by National Science Foundation under DEB 2027284. We thank Professor M. Francesca Cotrufo (Colorado State University) for her insightful comments and stimulating discussion that improved the manuscript. The National Ecological Observatory Network (NEON) is a program sponsored by the U.S. National Science Foundation and operated under cooperative agreement by Battelle. This material uses specimens and/or samples collected as part of the NEON Program. The 21 T FT-ICR mass spectrometer at the National High Magnetic Field Laboratory is located in the Ion Cyclotron

435 Resonance user facility, which is supported by the United States of America National Science Foundation

436 Division of Materials Research and Division of Chemistry through DMR-2128556 and the State of Florida.

437 **References**

438 1. J. Lehmann, M. Kleber, The contentious nature of soil organic matter. *Nature* **528**, 60–68 (2015).

439 2. C. Liang, J. P. Schimel, J. D. Jastrow, The importance of anabolism in microbial control over soil
440 carbon storage. *Nature Microbiology* **2**, 17105 (2017).

441 3. E. A. Davidson, I. A. Janssens, Temperature sensitivity of soil carbon decomposition and feedbacks
442 to climate change. *Nature* **440**, 165–173 (2006).

443 4. N. W. Sokol, *et al.*, Global distribution, formation and fate of mineral-associated soil organic matter
444 under a changing climate: A trait-based perspective. *Functional Ecology* **36**, 1411–1429 (2022).

445 5. B. Ahrens, *et al.*, Combination of energy limitation and sorption capacity explains 14C depth gradients.
446 *Soil Biology and Biochemistry* **148**, 107912 (2020).

447 6. L. Yu, B. Ahrens, T. Wutzler, M. Schrumpf, S. Zaehle, Jena Soil Model (JSM v1.0; revision 1934): a
448 microbial soil organic carbon model integrated with nitrogen and phosphorus processes. *Geosci.*
449 *Model Dev.* **13**, 783–803 (2020).

450 7. D. Woolf, J. Lehmann, Microbial models with minimal mineral protection can explain long-term soil
451 organic carbon persistence. *Scientific Reports* **9**, 6522 (2019).

452 8. Baohua. Gu, Juergen. Schmitt, Zhihong. Chen, Liyuan. Liang, J. F. McCarthy, Adsorption and
453 desorption of natural organic matter on iron oxide: mechanisms and models. *Environ. Sci. Technol.*
454 **28**, 38–46 (1994).

455 9. K. Kaiser, W. Zech, Release of Natural Organic Matter Sorbed to Oxides and a Subsoil. *Soil Science*
456 *Society of America Journal* **63**, 1157–1166 (1999).

457 10. M. Kleber, *et al.*, Dynamic interactions at the mineral–organic matter interface. *Nature Reviews Earth*
458 *& Environment* **2**, 402–421 (2021).

459 11. K. Georgiou, *et al.*, Global stocks and capacity of mineral-associated soil organic carbon. *Nature*
460 *Communications* **13**, 3797 (2022).

461 12. M. Kleber, *et al.*, “Chapter One - Mineral–Organic Associations: Formation, Properties, and
462 Relevance in Soil Environments” in *Advances in Agronomy*, D. L. Sparks, Ed. (Academic Press,
463 2015), pp. 1–140.

464 13. S. A. Schweizer, F. B. Bucka, M. Graf-Rosenfellner, I. Kögel-Knabner, Soil microaggregate size
465 composition and organic matter distribution as affected by clay content. *Geoderma* **355**, 113901
466 (2019).

14. K. U. Totsche, *et al.*, Microaggregates in soils. *Journal of Plant Nutrition and Soil Science* **181**, 104–136 (2018).

15. R. Z. Abramoff, *et al.*, Improved global-scale predictions of soil carbon stocks with Millennial Version 2. *Soil Biology and Biochemistry* **164**, 108466 (2022).

16. C. Moni, C. Rumpel, I. Virto, A. Chabbi, C. Chenu, Relative importance of sorption versus aggregation for organic matter storage in subsoil horizons of two contrasting soils. *European Journal of Soil Science* **61**, 958–969 (2010).

17. K. Heckman, *et al.*, Factors affecting the molecular structure and mean residence time of occluded organics in a lithosequence of soils under ponderosa pine. *Soil Biology and Biochemistry* **77**, 1–11 (2014).

18. K. Heckman, *et al.*, Beyond bulk: Density fractions explain heterogeneity in global soil carbon abundance and persistence. *Global Change Biology* **28**, 1178–1196 (2022).

19. M. von Lützow, *et al.*, SOM fractionation methods: Relevance to functional pools and to stabilization mechanisms. *Soil Biology and Biochemistry* **39**, 2183–2207 (2007).

20. C. M. Kallenbach, S. D. Frey, A. S. Grandy, Direct evidence for microbial-derived soil organic matter formation and its ecophysiological controls. *Nature Communications* **7**, 13630 (2016).

21. M. F. Cotrufo, M. D. Wallenstein, C. M. Boot, K. Denef, E. Paul, The Microbial Efficiency-Matrix Stabilization (MEMS) framework integrates plant litter decomposition with soil organic matter stabilization: do labile plant inputs form stable soil organic matter? *Global Change Biology* **19**, 988–995 (2013).

22. A. Miltner, P. Bombach, B. Schmidt-Brücken, M. Kästner, SOM genesis: microbial biomass as a significant source. *Biogeochemistry* **111**, 41–55 (2012).

23. M. Ludwig, *et al.*, Microbial contribution to SOM quantity and quality in density fractions of temperate arable soils. *Soil Biology and Biochemistry* **81**, 311–322 (2015).

24. M. J. Castellano, K. E. Mueller, D. C. Olk, J. E. Sawyer, J. Six, Integrating plant litter quality, soil organic matter stabilization, and the carbon saturation concept. *Global Change Biology* **21**, 3200–3209 (2015).

25. G. Angst, K. E. Mueller, I. Kögel-Knabner, K. H. Freeman, C. W. Mueller, Aggregation controls the stability of lignin and lipids in clay-sized particulate and mineral associated organic matter. *Biogeochemistry* **132**, 307–324 (2017).

26. M. G. Kramer, J. Sanderman, O. A. Chadwick, J. Chorover, P. M. Vitousek, Long-term carbon storage through retention of dissolved aromatic acids by reactive particles in soil. *Global Change Biology* **18**, 2594–2605 (2012).

27. G. Angst, K. E. Mueller, K. G. J. Nierop, M. J. Simpson, Plant- or microbial-derived? A review on the molecular composition of stabilized soil organic matter. *Soil Biology and Biochemistry* **156**, 108189 (2021).

28. K. Eusterhues, C. Rumpel, M. Kleber, I. Kögel-Knabner, Stabilisation of soil organic matter by interactions with minerals as revealed by mineral dissolution and oxidative degradation. *Organic Geochemistry* **34**, 1591–1600 (2003).

29. K. Eusterhues, C. Rumpel, I. Kögel-Knabner, Composition and radiocarbon age of HF-resistant soil organic matter in a Podzol and a Cambisol. *Organic Geochemistry* **38**, 1356–1372 (2007).

30. S. Spielvogel, J. Prietzel, I. Kögel-Knabner, Soil organic matter stabilization in acidic forest soils is preferential and soil type-specific. *European Journal of Soil Science* **59**, 674–692 (2008).

31. J. M. Lavallee, J. L. Soong, M. F. Cotrufo, Conceptualizing soil organic matter into particulate and mineral-associated forms to address global change in the 21st century. *Global Change Biology* **26**, 261–273 (2020).

32. S. Chen, *et al.*, Legacy Effects of Sorption Determine the Formation Efficiency of Mineral-Associated Soil Organic Matter. *Environ. Sci. Technol.* **56**, 2044–2053 (2022).

33. N. Fierer, R. B. Jackson, The diversity and biogeography of soil bacterial communities. *Proceedings of the National Academy of Sciences* **103**, 626–631 (2006).

34. R. L. Barnard, C. A. Osborne, M. K. Firestone, Responses of soil bacterial and fungal communities to extreme desiccation and rewetting. *The ISME Journal* **7**, 2229–2241 (2013).

35. N. W. Sokol, J. Sanderman, M. A. Bradford, Pathways of mineral-associated soil organic matter formation: Integrating the role of plant carbon source, chemistry, and point of entry. *Global Change Biology* **25**, 12–24 (2019).

36. K. Kaiser, K. Kalbitz, Cycling downwards – dissolved organic matter in soils. *Soil Biology and Biochemistry* **52**, 29–32 (2012).

37. K. Kalbitz, S. Solinger, J.-H. Park, B. Michalzik, E. Matzner, Controls on the dynamics of dissolved organic matter in soils: a review. *Soil science* **165**, 277–304 (2000).

38. D. S. Schimel, Drylands in the Earth System. *Science* **327**, 418–419 (2010).

39. E. K. Coward, T. Ohno, A. F. Plante, Adsorption and Molecular Fractionation of Dissolved Organic Matter on Iron-Bearing Mineral Matrices of Varying Crystallinity. *Environ. Sci. Technol.* **52**, 1036–1044 (2018).

40. Z. Hu, *et al.*, Controls of Mineral Solubility on Adsorption-Induced Molecular Fractionation of Dissolved Organic Matter Revealed by 21 T FT-ICR MS. *Environ. Sci. Technol.* **58**, 2313–2322 (2024).

41. K. Eusterhues, *et al.*, Fractionation of Organic Matter Due to Reaction with Ferrihydrite: Coprecipitation versus Adsorption. *Environ. Sci. Technol.* **45**, 527–533 (2011).

42. B. Berg, C. McClaugherty, *Plant litter: decomposition, humus formation, carbon sequestration* (Springer, 2008).

43. R. Sutton, G. Sposito, Molecular Structure in Soil Humic Substances: The New View. *Environ. Sci. Technol.* **39**, 9009–9015 (2005).

538 44. I. Kögel-Knabner, The macromolecular organic composition of plant and microbial residues as inputs
539 to soil organic matter. *Soil biology and biochemistry* **34**, 139–162 (2002).

540 45. N. DiDonato, H. Chen, D. Waggoner, P. G. Hatcher, Potential origin and formation for molecular
541 components of humic acids in soils. *Geochimica et Cosmochimica Acta* **178**, 210–222 (2016).

542 46. M. Kleber, P. Sollins, R. Sutton, A conceptual model of organo-mineral interactions in soils: self-
543 assembly of organic molecular fragments into zonal structures on mineral surfaces. *Biogeochemistry*
544 **85**, 9–24 (2007).

545 47. J. A. Baldock, C. A. Masiello, Y. Gélinas, J. I. Hedges, Cycling and composition of organic matter in
546 terrestrial and marine ecosystems. *Marine Chemistry* **92**, 39–64 (2004).

547 48. P. N. Nelson, J. A. Baldock, Estimating the molecular composition of a diverse range of natural
548 organic materials from solid-state 13C NMR and elemental analyses. *Biogeochemistry* **72**, 1–34
549 (2005).

550 49. R. G. Joergensen, Amino sugars as specific indices for fungal and bacterial residues in soil. *Biology*
551 *and Fertility of Soils* **54**, 559–568 (2018).

552 50. R. Kiem, I. Kögel-Knabner, Contribution of lignin and polysaccharides to the refractory carbon pool in
553 C-depleted arable soils. *Soil Biology and Biochemistry* **35**, 101–118 (2003).

554 51. G. Guggenberger, W. Zech, R. J. Thomas, Lignin and carbohydrate alteration in particle-size
555 separates of an oxisol under tropical pastures following native savanna. *Soil Biology and Biochemistry*
556 **27**, 1629–1638 (1995).

557 52. A. Gunina, Y. Kuzyakov, Sugars in soil and sweets for microorganisms: Review of origin, content,
558 composition and fate. *Soil Biology and Biochemistry* **90**, 87–100 (2015).

559 53. W. Amelung, S. Brodowski, A. Sandhage-Hofmann, R. Bol, “Chapter 6 Combining Biomarker with
560 Stable Isotope Analyses for Assessing the Transformation and Turnover of Soil Organic Matter” in
561 *Advances in Agronomy*, (Academic Press, 2008), pp. 155–250.

562 54. G. Gleixner, N. Poirier, R. Bol, J. Balesdent, Molecular dynamics of organic matter in a cultivated soil.
563 *Organic Geochemistry* **33**, 357–366 (2002).

564 55. K. Kalbitz, *et al.*, Changes in properties of soil-derived dissolved organic matter induced by
565 biodegradation. *Soil Biology and Biochemistry* **35**, 1129–1142 (2003).

566 56. K. Kaiser, G. Guggenberger, The role of DOM sorption to mineral surfaces in the preservation of
567 organic matter in soils. *Organic Geochemistry* **31**, 711–725 (2000).

568 57. E. D. Whalen, *et al.*, Clarifying the evidence for microbial- and plant-derived soil organic matter, and
569 the path toward a more quantitative understanding. *Global Change Biology* **28**, 7167–7185 (2022).

570 58. M. Spohn, Preferential adsorption of nitrogen-and phosphorus-containing organic compounds to
571 minerals in soils: A review. *Soil Biology and Biochemistry* 109428 (2024).

59. G. GUGGENBERGER, B. T. CHRISTENSEN, W. ZECH, Land-use effects on the composition of organic matter in particle-size separates of soil: I. Lignin and carbohydrate signature. *European Journal of Soil Science* **45**, 449–458 (1994).

60. I. Kögel-Knabner, *et al.*, Organo-mineral associations in temperate soils: Integrating biology, mineralogy, and organic matter chemistry. *Journal of Plant Nutrition and Soil Science* **171**, 61–82 (2008).

61. J. Prietzel, *et al.*, Comparison of soil organic carbon speciation using C NEXAFS and CPMAS 13C NMR spectroscopy. *Science of The Total Environment* **628–629**, 906–918 (2018).

62. G. Janusz, *et al.*, Lignin degradation: microorganisms, enzymes involved, genomes analysis and evolution. *FEMS Microbiology Reviews* **41**, 941–962 (2017).

63. S. J. Hall, C. Ye, S. R. Weintraub, W. C. Hockaday, Molecular trade-offs in soil organic carbon composition at continental scale. *Nature Geoscience* **13**, 687–692 (2020).

64. H.-R. Mao, *et al.*, Dual role of silt and clay in the formation and accrual of stabilized soil organic carbon. *Soil Biology and Biochemistry* **192**, 109390 (2024).

65. M. Kästner, A. Miltner, S. Thiele-Bruhn, C. Liang, Microbial Necromass in Soils—Linking Microbes to Soil Processes and Carbon Turnover. *Frontiers in Environmental Science* **Volume 9-2021** (2021).

66. T. Camenzind, K. Mason-Jones, I. Mansour, M. C. Rillig, J. Lehmann, Formation of necromass-derived soil organic carbon determined by microbial death pathways. *Nature Geoscience* **16**, 115–122 (2023).

67. N. W. Sokol, M. A. Bradford, Microbial formation of stable soil carbon is more efficient from belowground than aboveground input. *Nature Geoscience* **12**, 46–53 (2019).

68. Y. Zhang, *et al.*, Simulating measurable ecosystem carbon and nitrogen dynamics with the mechanistically defined MEMS 2.0 model. *Biogeosciences* **18**, 3147–3171 (2021).

69. K. Georgiou, *et al.*, Soil Carbon Saturation: What Do We Really Know? *Global Change Biology* **31**, e70197 (2025).

70. G. Angst, *et al.*, Unlocking complex soil systems as carbon sinks: multi-pool management as the key. *Nature Communications* **14**, 2967 (2023).

71. J. Six, H. Bossuyt, S. Degryze, K. Denef, A history of research on the link between (micro)aggregates, soil biota, and soil organic matter dynamics. *Soil and Tillage Research* **79**, 7–31 (2004).

72. J. Six, E. T. Elliott, K. Paustian, Soil macroaggregate turnover and microaggregate formation: a mechanism for C sequestration under no-tillage agriculture. *Soil Biology and Biochemistry* **32**, 2099–2103 (2000).

73. Y. Jia, *et al.*, Plant and microbial pathways driving plant diversity effects on soil carbon accumulation in subtropical forest. *Soil Biology and Biochemistry* **161**, 108375 (2021).

74. G. W. D. Ferreira, *et al.*, Retaining eucalyptus harvest residues promotes different pathways for particulate and mineral-associated organic matter. *Ecosphere* **12**, e03439 (2021).

75. C. Rumpel, I. Kögel-Knabner, Deep soil organic matter—a key but poorly understood component of terrestrial C cycle. *Plant and Soil* **338**, 143–158 (2011).

76. G. Angst, *et al.*, Conceptualizing soil fauna effects on labile and stabilized soil organic matter. *Nature Communications* **15**, 5005 (2024).

77. V. Alcántara, A. Don, R. Well, R. Nieder, Deep ploughing increases agricultural soil organic matter stocks. *Global Change Biology* **22**, 2939–2956 (2016).

78. A. S. Thorpe, *et al.*, Introduction to the sampling designs of the National Ecological Observatory Network Terrestrial Observation System. *Ecosphere* **7**, e01627 (2016).

79. P. M. Hansen, *et al.*, Distinct, direct and climate-mediated environmental controls on global particulate and mineral-associated organic carbon storage. *Global Change Biology* **30**, e17080 (2024).

80. M. G. Kramer, O. A. Chadwick, Climate-driven thresholds in reactive mineral retention of soil carbon at the global scale. *Nature Climate Change* **8**, 1104–1108 (2018).

81. S. Leuthold, M. Haddix, J. Lavallee, M. Cotrufo, Physical Fractionation Techniques, Reference Module in Earth Systems and Environmental Sciences. (2022).

82. D. Harris, W. R. Horwáth, C. Van Kessel, Acid fumigation of soils to remove carbonates prior to total organic carbon or carbon-13 isotopic analysis. *Soil Science Society of America Journal* **65**, 1853–1856 (2001).

83. T. Dittmar, B. Koch, N. Hertkorn, G. Kattner, A simple and efficient method for the solid-phase extraction of dissolved organic matter (SPE-DOM) from seawater. *Limnology and Oceanography: Methods* **6**, 230–235 (2008).

84. D. F. Smith, D. C. Podgorski, R. P. Rodgers, G. T. Blakney, C. L. Hendrickson, 21 Tesla FT-ICR Mass Spectrometer for Ultrahigh-Resolution Analysis of Complex Organic Mixtures. *Anal. Chem.* **90**, 2041–2047 (2018).

85. C. L. Hendrickson, *et al.*, 21 Tesla Fourier Transform Ion Cyclotron Resonance Mass Spectrometer: A National Resource for Ultrahigh Resolution Mass Analysis. *J. Am. Soc. Mass Spectrom.* **26**, 1626–1632 (2015).

86. G. T. Blakney, C. L. Hendrickson, A. G. Marshall, Predator data station: A fast data acquisition system for advanced FT-ICR MS experiments. *International Journal of Mass Spectrometry* **306**, 246–252 (2011).

87. T. Chen, S. C. Beu, N. K. Kaiser, C. L. Hendrickson, Note: Optimized circuit for excitation and detection with one pair of electrodes for improved Fourier transform ion cyclotron resonance mass spectrometry. *Review of Scientific Instruments* **85**, 066107 (2014).

88. N. K. Kaiser, A. M. McKenna, J. J. Savory, C. L. Hendrickson, A. G. Marshall, Tailored Ion Radius Distribution for Increased Dynamic Range in FT-ICR Mass Analysis of Complex Mixtures. *Anal. Chem.* **85**, 265–272 (2013).

89. J. J. Savory, *et al.*, Parts-Per-Billion Fourier Transform Ion Cyclotron Resonance Mass Measurement Accuracy with a “Walking” Calibration Equation. *Anal. Chem.* **83**, 1732–1736 (2011).

90. R. L. Sleighter, Z. Liu, J. Xue, P. G. Hatcher, Multivariate Statistical Approaches for the Characterization of Dissolved Organic Matter Analyzed by Ultrahigh Resolution Mass Spectrometry. *Environ. Sci. Technol.* **44**, 7576–7582 (2010).

91. K. Boye, *et al.*, Thermodynamically controlled preservation of organic carbon in floodplains. *Nature Geoscience* **10**, 415–419 (2017).

92. T. Wang, A. Hamann, D. Spittlehouse, C. Carroll, Locally downscaled and spatially customizable climate data for historical and future periods for North America. *PloS one* **11**, e0156720 (2016).

93. G. H. Hargreaves, Z. A. Samani, Reference crop evapotranspiration from temperature. *Applied engineering in agriculture* **1**, 96–99 (1985).

94. H. Hotelling, *Contributions to probability and statistics: essays in honor of Harold Hotelling* (Stanford University Press, 1960).

95. S. Shaphiro, M. Wilk, An analysis of variance test for normality. *Biometrika* **52**, 591–611 (1965).

96. J. W. Tukey, Comparing individual means in the analysis of variance. *Biometrics* 99–114 (1949).

97. J. S. Lefcheck, piecewiseSEM: Piecewise structural equation modelling in r for ecology, evolution, and systematics. *Methods in Ecology and Evolution* **7**, 573–579 (2016).

98. J. B. Grace, *et al.*, Integrative modelling reveals mechanisms linking productivity and plant species richness. *Nature* **529**, 390–393 (2016).

Figures and Tables

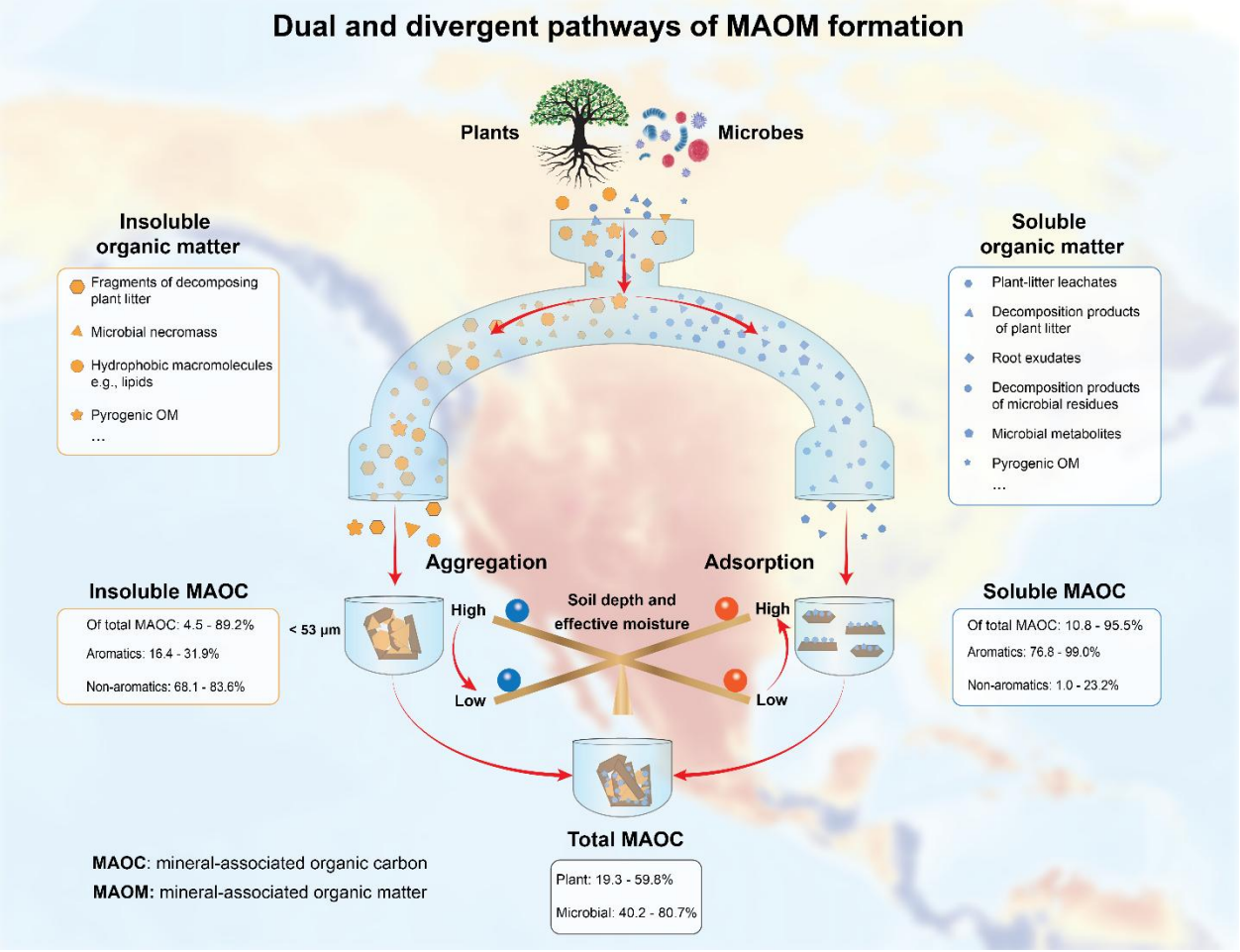

Fig. 1. A conceptual model showing dual and divergent pathways for the formation of mineral-associated organic matter (MAOM) in soils. MAOM can form via two primary pathways: 1) adsorption of dissolved organic matter (DOM) onto mineral surfaces, and 2) aggregation or attachment of insoluble organic matter with mineral particles within microaggregates (<53 μm). Both plant- and microbial-derived inputs contribute to carbon associated with each pathway. Aggregation and attachment stabilize fine particulate organic matter, including decomposing plant litter fragments, microbial necromass, hydrophobic macromolecules (e.g., lipids), pyrogenic organic matter, etc. In contrast, adsorption involves DOM consisting of plant litter leachates, decomposition products of plant and microbial residues, root exudates, microbial metabolites

such as extracellular polymeric substances (EPS), pyrogenic organic matter, etc. The present study quantified the relative contributions of adsorption (soluble C) and aggregation/attachment (insoluble C) pathways to MAOM formation and characterized the composition of the associated C across diverse terrestrial ecosystems at the continental scale. Soil depth and effective moisture are key environmental factors that regulate the relative contributions of adsorption and aggregtion/attahchment pathways to MAOM formation.

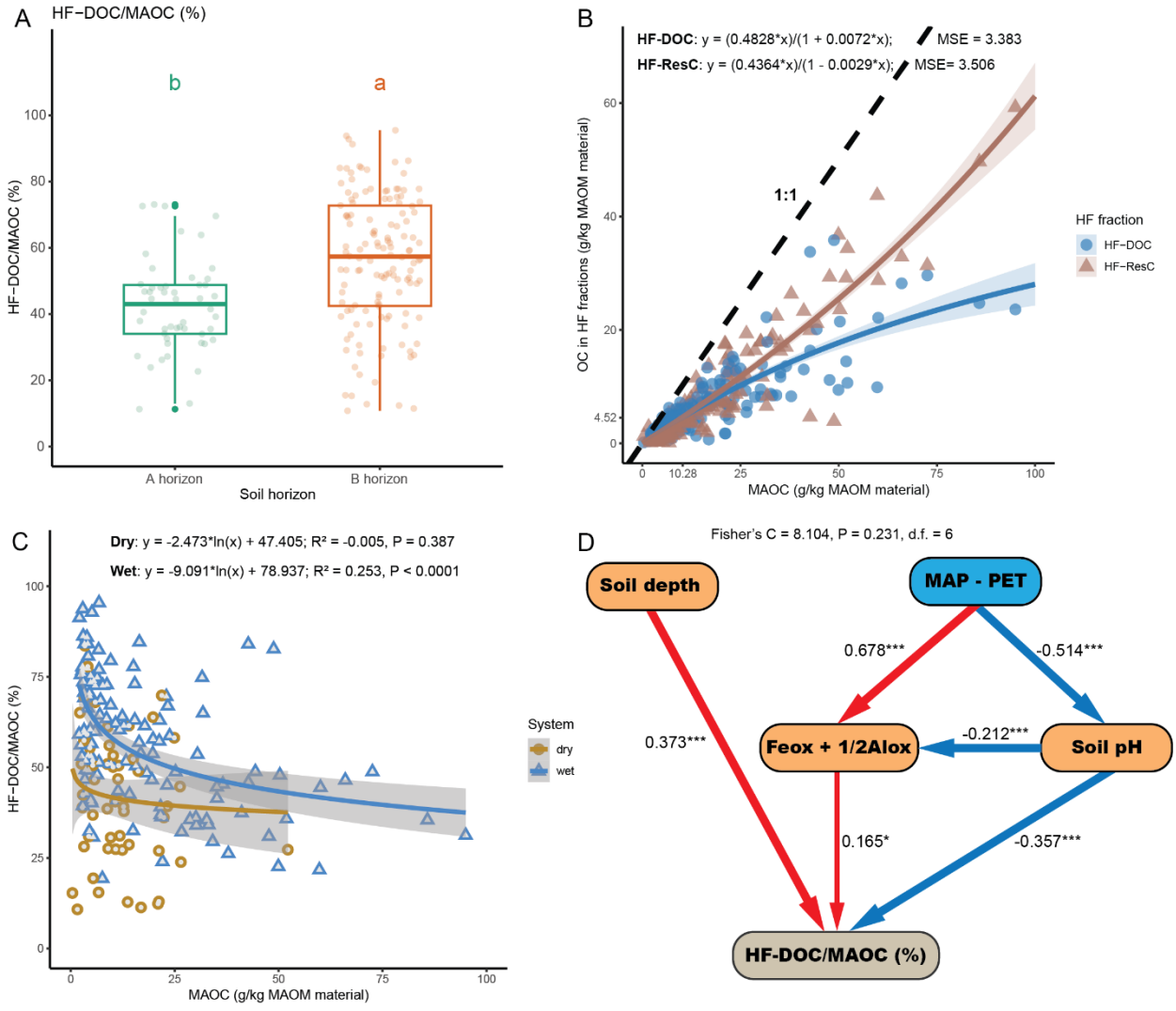

697

698 **Fig. 2.** The relative contributions of HF-DOC and HF-ResC to MAOC, and their key controlling
699 environmental drivers. (A) The relative contribution (HF-DOC/MAOC, %) of hydrofluoric acid (HF)-extracted
700 dissolved organic C (HF-DOC) to mineral-associated organic C (MAOC) in the A and B horizon soils. (B)
701 The correlations between HF-DOC or HF-extraction residue C (HF-ResC) and MAOC concentrations in
702 g/kg MAOM material (i.e., MAOC + silt +clay). (C) The correlation between HF-DOC/MAOC (%) and MAOC
703 concentrations in g/kg MAOM material. (D) A structural equation model illustrating the environmental factors
704 influencing HF-DOC/MAOC (%). In the boxplot, the box represents the first and third quartiles, the whiskers

indicate the minimum and maximum values, the horizontal line represents the median, and different lowercase letters denote statistically significant differences. In Figure b, the blue and brown lines represent the Langmuir adsorption model fit. In panel c, the blue and brown line show logarithmic fits, while the gray band represents the 95% confidence intervals. In panel d, solid arrows represent significant pathways, with red arrows indicating positive piecewise relationships and blue arrows indicating negative piecewise relationships. The width of the arrows corresponds to the strength of the causal relationships. Numbers on the arrows denote standardized path coefficients, with significance levels represented as follows: *$p < 0.05$, **$p < 0.01$, and ***$p < 0.001$. MSE: mean square error; MAOM material: the sum of the mass of MAOC, silt, and clay. MAP: mean annual precipitation; PET: potential evapotranspiration; Feox + 1/2Alox: a sum of oxalate-extractable Fe and Al, and only half of the extracted Al is considered.

730

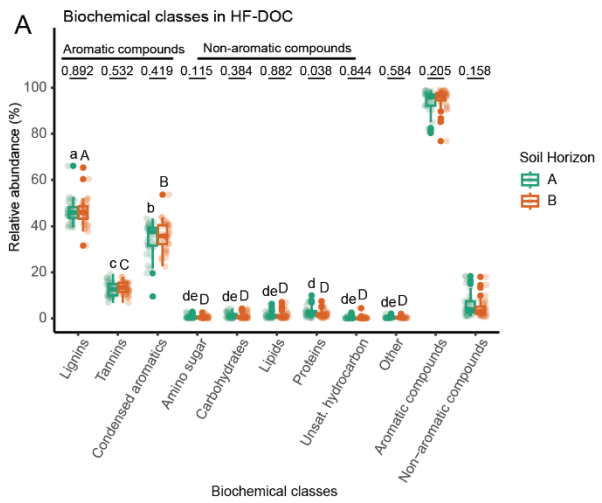
A
Biochemical classes in HF-DOC
Aromatic compounds
Non-aromatic compounds
0.892 0.532 0.419 0.115 0.384 0.882 0.038 0.844 0.584 0.205 0.158
Relative abundance (%)
Soil Horizon
A
B
Lignins
Tannins
Condensed aromatics
Amino sugar
Carbohydrates
Lipids
Proteins
Unsat. hydrocarbon
Other
Aromatic compounds
Non-aromatic compounds
Biochemical classes

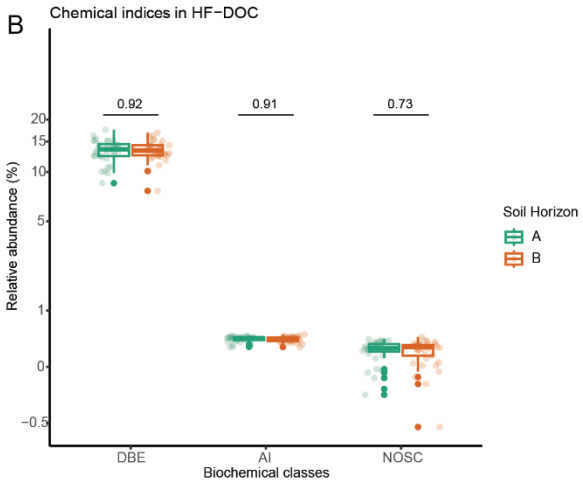
B
Chemical indices in HF−DOC
0.92
0.91
0.73
Relative abundance (%)
Soil Horizon
A
B
DBE
AI
NOSC
Biochemical classes

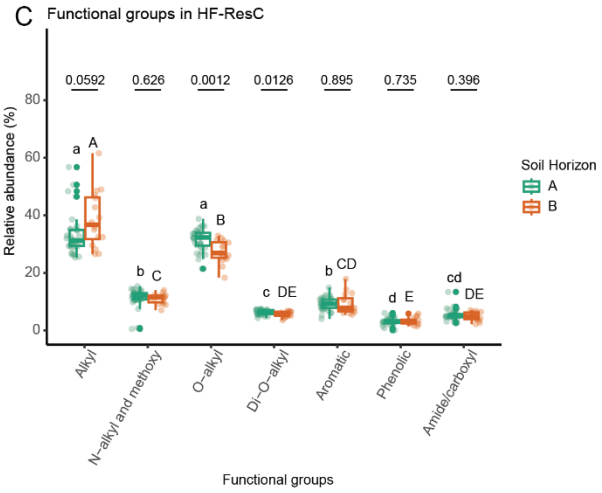
C
Functional groups in HF-ResC
0.0592 0.626 0.0012 0.0126 0.895 0.735 0.396
Relative abundance (%)
Soil Horizon
A
B
Alkyl
N−alkyl and methoxy
O−alkyl
Di−O−alkyl
Aromatic
Phenolic
Amide/carboxyl
Functional groups

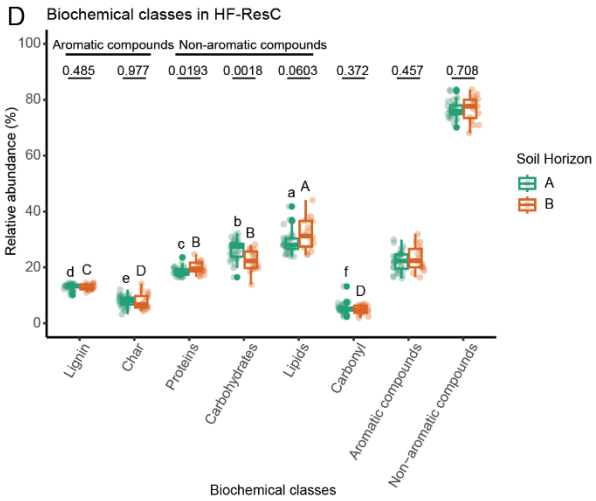
D
Biochemical classes in HF-ResC
Aromatic compounds
Non-aromatic compounds
0.485 0.977 0.0193 0.0018 0.0603 0.372 0.457 0.708
Relative abundance (%)
Soil Horizon
A
B
Lignin
Char
Proteins
Carbohydrates
Lipids
Carbonyl
Aromatic compounds
Non-aromatic compounds
Biochemical classes

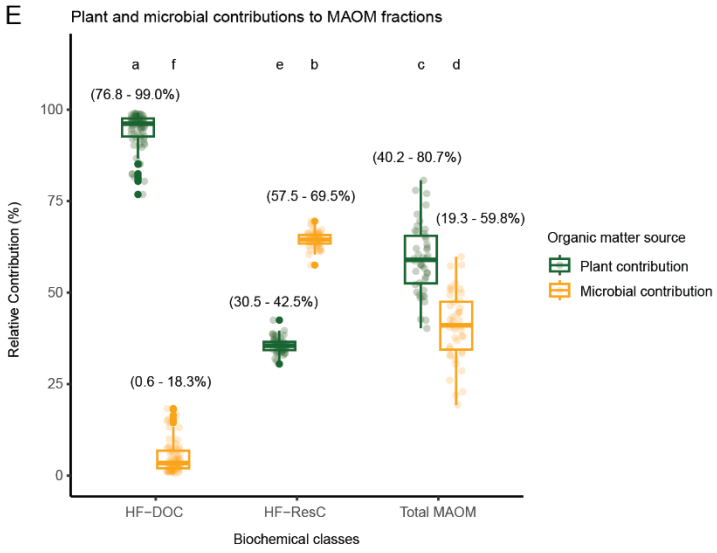
E
Plant and microbial contributions to MAOM fractions
(76.8 - 99.0%)
(0.6 - 18.3%)
(57.5 - 69.5%)
(30.5 - 42.5%)
(40.2 - 80.7%)
(19.3 - 59.8%)
Relative Contribution (%)
Organic matter source
Plant contribution
Microbial contribution
HF−DOC
HF−ResC
Total MAOM
Biochemical classes

Fig. 3. The chemical composition and properties of HF-DOC and HF-ResC. (A) The relative abundance of different biochemical classes in HF-DOC, characterized by FT-ICR-MS, in the A and B horizon soils. (B) Chemical indices in HF-DOC based on FT-ICR-MS data, including double bond equivalent (DBE), aromaticity index (AI), and nominal oxidation state of carbon (NOSC). (C) The relative abundance of different functional groups in HF-ResC in the A and B horizon soils, characterized by solid-state NMR spectroscopy. (D) The relative abundance of various biochemical classes in HF-ResC derived from a mixing model. Biochemical classes in HF-DOC include lignin, tannin, condensed aromatic compounds, amino sugars, carbohydrates, lipids, proteins, and unsaturated hydrocarbons. (E) The relative contribution of plant and microbial sources to different MAOM fractions, including HF-DOC, HF-ResC, and total MAOM. Aromatic compounds = lignin + tannin + condensed aromatics. Biochemical classes in HF-ResC include lignin, char, protein, carbohydrates, lipids, and carbonyl. Non-aromatic compounds = lipids + carbohydrates + proteins + ½ carbonyl. In the boxplot, the box represents the first and third quartiles, the whiskers indicate the minimum and maximum values, the horizontal line represents the median, and solid dots represent outliers. Different lowercase letters indicate statistically significant differences in the relative abundance of biochemical classes in the A horizon, while different uppercase letters indicate statistically significant differences in the B horizon. The numbers above each group denote the P-value, with $P < 0.05$ indicating a statistically significant difference.

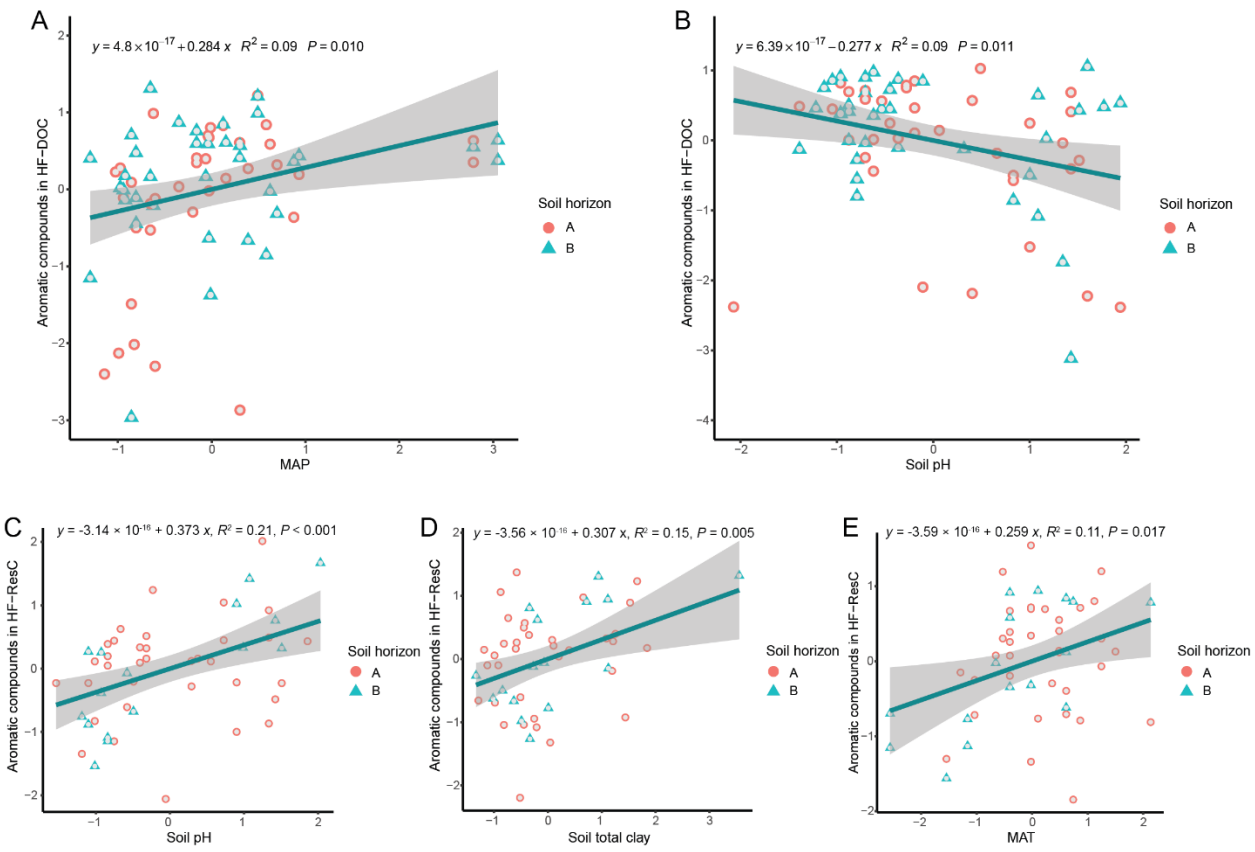

Fig. 4. Key environmental factors shaping the relative abundance of aromatic compounds in HF-DOC and HF-ResC. (A) Multivariate partial plots showing correlations between the relative abundance of aromatic compounds in HF-DOC and mean annual precipitation (MAP). (B) Multivariate partial plots showing correlations between the relative abundance of aromatic compounds in HF-DOC and soil pH. (C) Multivariate partial plots showing correlations between the relative abundance of aromatic compounds in HF-ResC and soil pH. (D) Multivariate partial plots showing correlations between the relative abundance of aromatic compounds in HF-ResC and clay content. (E) Multivariate partial plots showing correlations between the relative abundance of aromatic compounds in HF-ResC and mean annual temperature (MAT). Functional groups: alkyl, N-alkyl/methoxy, O-alkyl, Di-O-alkyl, aromatic, phenolic, and amide/carboxyl. HF-DOC biochemical classes: lignin, tannin, condensed aromatics, amino sugars, carbohydrates, lipids, proteins, and unsaturated hydrocarbons; aromatic compounds = lignin + tannin + condensed aromatics.

HF-ResC classes: lignin, char, protein, carbohydrates, lipids, and carbonyl; non-aromatic compounds = lipids + carbohydrates + proteins + ½ carbonyl. Green lines indicate linear fits; gray bands represent 95% confidence intervals.